

SDCoNet: Saliency-Driven Multi-Task Collaborative Network for Remote Sensing Object Detection

Ruo Qi, Linhui Dai*, Yusong Qin, Chaolei Yang, Yanshan Li

Abstract—In remote sensing images, complex backgrounds, weak object signals, and small object scales make accurate detection particularly challenging, especially under low-quality imaging conditions. A common strategy is to integrate single-image super-resolution (SR) before detection; however, such serial pipelines often suffer from misaligned optimization objectives, feature redundancy, and a lack of effective interaction between SR and detection. To address these issues, we propose a Saliency-Driven multi-task Collaborative Network (SDCoNet) that couples SR and detection through implicit feature sharing while preserving task specificity. SDCoNet employs the swin transformer-based shared encoder, where hierarchical window-shifted self-attention supports cross-task feature collaboration and adaptively balances the trade-off between texture refinement and semantic representation. In addition, a multi-scale saliency prediction module produces importance scores to select key tokens, enabling focused attention on weak object regions, suppression of background clutter, and suppression of adverse features introduced by multi-task coupling. Furthermore, a gradient routing strategy is introduced to mitigate optimization conflicts. It first stabilizes detection semantics and subsequently routes SR gradients along a detection-oriented direction, enabling the framework to guide the SR branch to generate high-frequency details that are explicitly beneficial for detection. Experiments on public datasets, including NWPU VHR-10-Split, DOTAv1.5-Split, and HRSSD-Split, demonstrate that the proposed method, while maintaining competitive computational efficiency, significantly outperforms existing mainstream algorithms in small object detection on low-quality remote sensing images. Our code is available at <https://github.com/qiruo-ya/SDCoNet>.

Index Terms—Remote sensing object detection, Super-resolution, Multi-task learning, Swin transformer, Small object detection.

I. INTRODUCTION

OBJECT detection in remote sensing aims to identify and locate ground objects from aerial or satellite imagery, serving as a fundamental task in Earth observation. Despite the increasing accessibility of high-resolution data, diverse imaging conditions and complex scenes often result in cluttered backgrounds, weak feature responses, and significant

This work was partially supported by National Natural Science Foundation of China (No.62471317), Natural Science Foundation of Shenzhen (No. JCYJ20240813141331042), Guangdong Provincial Key Laboratory (Grant 2023B1212060076), and the Scientific Foundation for Youth Scholars of Shenzhen University, China. (*Corresponding author: Linhui Dai).

Ruo Qi, Linhui Dai, Yusong Qin, Chaolei Yang, Yanshan Li are with the Institute of Intelligent Information Processing, Shenzhen University, Guangdong Key Laboratory of Intelligent Information Processing, Shenzhen and Shenzhen Key Laboratory of Modern Communications and Information Processing, Shenzhen University, Shenzhen, China 518000, China (email: qiruo2023@email.szu.edu.cn; dailinhui@szu.edu.cn; 2450042012@mails.szu.edu.cn; yangchaolei2022@email.szu.edu.cn; lys@szu.edu.cn)

scale variations. Such inherent difficulties amplify ambiguity in feature discrimination, posing severe challenges for accurately differentiating sparse objects from homogeneous surface textures [1], [2].

To enhance fine details and provide clearer inputs for detection, single-image super-resolution (SR) [3]–[6] has been integrated into remote sensing pipelines. While early works treated SR as an independent pre-processing module, recent trends are shifting toward tightly coupled multi-task frameworks that jointly optimize image reconstruction and object detection to alleviate information loss [7], [8]. However, most existing frameworks still follow a rigid sequential paradigm, which leads to a misalignment between pixel-level fidelity (e.g., PSNR) and detection-oriented semantic representations. This lack of explicit interaction reveals two critical bottlenecks: (1) **Inefficient Task Coordination**: SR and detection are driven by disparate supervision signals, making the shared representations prone to gradient conflicts and optimization bias toward a single task [9], [10]. (2) **Inadequate Adaptive Perception**: Despite overall quality improvements, existing detectors struggle to focus on salient regions corresponding to small objects. The feature distribution shift caused by SR reconstruction often weakens the compatibility between restored details and the query mechanisms of Transformer-based detectors [11]–[13], leading to systematic omissions in cluttered scenes.

From a representational perspective, these limitations stem from two fundamental mismatches: the Task-specific Objective Mismatch and the Spatial Attention Mismatch. First, as illustrated by the activation map visualizations in Fig. 1, SR prioritizes frequency-domain reconstruction to enhance textures, whereas detection relies on spatial semantic representations. To balance performance and efficiency, some approaches adopt a shared backbone to simultaneously encode both dense pixel-level details and sparse instance semantics. However, such forced integration often permits non-informative high-frequency noise or background textures, which are primarily favored by the SR branch, to interfere with the detection branch [3], [4]. This phenomenon leads to severe feature pollution, where object-relevant semantic representations are corrupted by task-irrelevant reconstruction details. Second, the blurring of salient regions in low-quality images exposes the inability of current architectures to effectively focus on small objects. CNN-based detectors [14]–[17] are often constrained by local receptive fields, while Transformer-based methods [11]–[13], [18]–[20] tend to diffuse attention over large homogeneous regions. These identified deficiencies underscore the need for a more synergistic SR-detection integration.

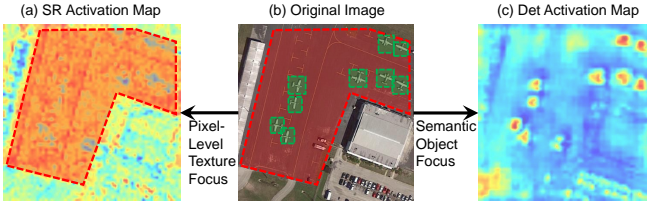


Fig. 1. **Visualization of activation maps for different tasks.** Fig. 1 (a) shows activation maps of the super-resolution task, which mainly attends to pixel-level texture and edge details, while Fig. 1 (c) shows activation maps of the object detection task, which primarily focuses on high-level semantic structures and object regions.

To address these issues, we propose the Saliency-Driven multi-task Collaborative Network (SDCoNet). Specifically designed for small object detection in low-quality imagery, SDCoNet replaces the traditional serial paradigm with a deep collaboration mechanism that systematically resolves the aforementioned mismatches. To reconcile the objective conflict between reconstruction and semantic discrimination, we implement an implicit feature sharing paradigm that ensures multi-task compatibility. Concurrently, a saliency-driven mechanism is introduced to rectify attention diffusion, thereby enabling the model to dynamically concentrate on potential object regions and addressing the spatial attention mismatch. These components are further harmonized by a gradient routing strategy, which stabilizes detection semantics before guiding the SR branch to generate high-frequency details that are explicitly beneficial for detection.

Our contributions are summarized as follows:

- 1) We propose an implicit feature sharing paradigm that enables semantically consistent collaboration between SR and detection tasks, breaking the limits of traditional serial learning.
- 2) A saliency-driven query token selection mechanism is introduced, enabling the network to dynamically focus on small object regions and suppress feature pollution caused by multi-task coupling.
- 3) We develop a gradient routing strategy to alleviate optimization conflicts, guiding the SR branch to generate high-frequency information beneficial for detection.
- 4) Extensive experiments demonstrate that SDCoNet achieves state-of-the-art performance on the NWPU VHR-10-Split [21], DOTAv1.5-Split [22], and HRSSD-Split datasets [23].

II. RELATED WORK

A. Image Super-Resolution

Image super-resolution (SR) plays a crucial role in small object detection by reconstructing fine details from low-resolution (LR) inputs, thereby enhancing feature discriminability for downstream recognition tasks. According to the underlying network architecture, existing SR methods can be broadly categorized into CNN-based and Transformer-based approaches.

CNN-Based: Following the seminal work of SRCNN [24], CNN-based SR methods have achieved remarkable progress

in image reconstruction [25]–[29]. These methods typically enhance feature expression through attention mechanisms, such as channel attention [30] and holistic attention [31] used to improve feature selection capability, while self-similarity attention [32] and non-local sparse attention [33] further introduce global dependencies to enhance context modeling. Despite their progress, CNNs are inherently constrained by local receptive fields. While non-local modeling attempts to mitigate this, it introduces prohibitive computational costs, leading to an unresolved trade-off between global semantic modeling and reconstruction efficiency in remote sensing scenarios.

Transformer-Based: Transformer, with its advantage in long-range dependency modeling through self-attention mechanisms, has demonstrated stronger feature expression capability in super-resolution tasks [34]–[36]. Liang et al. [37] proposed the SwinIR model, combining hierarchical feature extraction and reconstruction modules, achieving tasks such as super-resolution, denoising, and compression artifact removal. Xiao et al. [38] designed the TTST model with dynamic token selection and multi-scale feed-forward layers, effectively reducing redundant computation and improving reconstruction accuracy. Kang et al. [39] proposed ESTNet, which significantly reduces computational complexity while ensuring performance through efficient channel attention and residual group mechanisms. Overall, Transformer structures achieve a better balance between global feature modeling and efficiency, providing new ideas for remote sensing image super-resolution tasks.

B. Object Detection

Traditional CNN-based object detection methods are generally divided into two-stage and one-stage approaches. Two-stage methods (such as Faster R-CNN [14]) achieve high accuracy through region proposal and classification refinement, while one-stage methods (such as the YOLO series [15]) directly regress bounding boxes to improve inference speed. However, in remote sensing images, their performance remains limited due to small object sizes, arbitrary orientations, and complex backgrounds.

To address these challenges, numerous CNN-based frameworks have been proposed for remote sensing object detection. Some methods focus on enhancing feature representation and multiscale fusion, such as MS-OPN [40] and FSANet [41], which improve multi-level feature extraction and alignment to better capture small and densely distributed objects. Others emphasize context modeling and attention mechanisms to suppress background interference and enhance discriminative regions, including FE-CenterNet [42] and FFCA-YOLO [16]. Meanwhile, lightweight detectors such as LSODNet [17] optimize efficiency via depthwise and deformable convolutions. In this context, LEGNet [43] proposes a lightweight backbone that incorporates edge priors and Gaussian-based modeling to improve feature robustness in low-quality remote sensing images.

Recently, Transformer-based detectors have gained increasing attention due to their global modeling capabilities. PR-Deformable DETR [44] combines adaptive feature fusion and

deformable attention for multiscale and rotation-robust detection, achieving state-of-the-art results on several benchmark datasets. Drone-DETR [18] further optimizes the Transformer architecture for UAV onboard applications, balancing accuracy and real-time inference efficiency. Despite these advancements, small object detection in remote sensing remains challenging, particularly under low resolution and limited computational resources. Future work thus continues to explore lightweight, context-aware, and saliency-driven detection frameworks to further improve detection robustness and efficiency.

C. Multi-Task Learning for Super-Resolution and Object Detection Tasks

Recent research on joint SR and object detection for remote sensing images has focused on three approaches: stepwise learning [45], [46], joint optimization [9], [10], and selective optimization [47]. These methods aim to enhance image quality and improve detection performance, addressing challenges like weak feature responses and complex backgrounds.

Stepwise learning treats SR as an independent preprocessing step before object detection in remote sensing images, aiming to enhance image quality before detection tasks [45], [46]. This approach is simple and facilitates training, but lacks closed-loop optimization between SR and detection. As a result, while SR may improve image clarity, it does not necessarily enhance detection performance and can even introduce artifacts like pseudo-textures that negatively affect detection results.

Joint optimization strategies integrate super-resolution and object detection into a unified end-to-end framework [9], [10]. Unlike independent stepwise training, this paradigm constructs a serial SR-detection pipeline, allowing gradients from the detection loss to propagate back to the upstream SR module. Consequently, image reconstruction is guided by both pixel fidelity and downstream semantic needs, encouraging the recovery of object-relevant details. However, the intrinsic conflict between pixel-level fidelity and semantic-level invariance can lead to gradient inconsistency, hindering convergence and limiting the overall performance improvement.

Selective optimization, through region extraction or attention mechanisms, applies super-resolution only to key regions in remote sensing images, balancing efficiency and performance. The HSOD-Net framework proposed by Wu et al. [47] focuses super-resolution on potential object regions predicted by keypoints, achieving effective collaborative optimization of image enhancement and object detection. However, HSOD-Net still follows a step-wise pipeline in which the region selection is predicted on low-resolution features and then used to crop patches for subsequent super-resolution. Once the first-stage keypoint prediction misses or mislocalizes an object, the subsequent super-resolution module can no longer compensate for this error, leading to irreversible detection failures. Moreover, the hard region cropping and loosely coupled feature sharing make the interaction between enhancement and detection relatively shallow, so the detection loss provides only indirect feedback to the super-resolution branch.

Overall, although existing methods achieve collaborative optimization of SR and object detection tasks to varying

degrees, they still face problems such as inefficient feature sharing and optimization conflicts. How to enable tighter, detection-driven collaboration between super-resolution and object detection under an end-to-end optimization framework, while explicitly improving small object detection performance in remote sensing images and maintaining computational efficiency, remains a key research direction.

III. METHODS

A. Overview

To achieve synergistic collaboration between pixel-level detail recovery and object-level semantic abstraction, we propose the Saliency-Driven multi-task Collaborative Network (SDCoNet). This framework establishes a unified dual-branch architecture anchored by a cross-task parameter-shared encoder, facilitating the simultaneous optimization of pixel-level reconstruction and object-level recognition.

As illustrated in Fig. 2, The entire processing pipeline begins with the input low-resolution image I_{LR} . First, generalized multi-scale features are extracted through a shared encoder based on the Swin Transformer. Subsequently, these features are fed into two specialized paths: the SR branch utilizes a U-Net-style decoder to restore high-frequency details and output a high-resolution image I_{SR} . Simultaneously, the detection branch introduces a saliency-driven mechanism to dynamically filter query tokens. This filtering strategy focuses computational resources on critical regions, thereby enhancing the perception of small objects. Finally, the DINO-based [48] decoder outputs the specific categories and bounding box coordinates of the objects. Through this multi-task synergy, SDCoNet effectively suppresses background interference and achieves high-precision detection without introducing redundant inference overhead.

Furthermore, to resolve the optimization conflict between the two tasks, we propose a “Gradient Routing Strategy”. This strategy decouples the training trajectory into two phases: “Semantic Stabilization” (Stage 1) and “Collaborative Synergy” (Stage 2). By initially freezing the SR branch, we establish a robust semantic prior, subsequent joint training routes gradients from both tasks to the shared encoder, ensuring that the restored details are semantically discriminative.

B. Cross-Task Parameter Shared Encoder

We construct a cross-task parameter-shared encoder following the Swin Transformer Tiny (Swin-T) architecture [49], which serves as the foundational feature extraction module for both super-resolution and detection tasks. As illustrated by the four blue boxes in Fig. 2, the encoder comprises four hierarchical stages, each containing a Swin block that stacks multiple Swin Transformer layers (as shown in the right part of Fig. 2). Within each Swin Transformer layer, window-based multi-head self-attention (W-MSA) and shifted window multi-head self-attention (SW-MSA) are alternately applied to capture both local contextual information and long-range dependencies.

Given an input low-resolution image $I_{LR} \in \mathbb{R}^{H \times W \times 3}$, where H and W denote the spatial dimensions, the shared

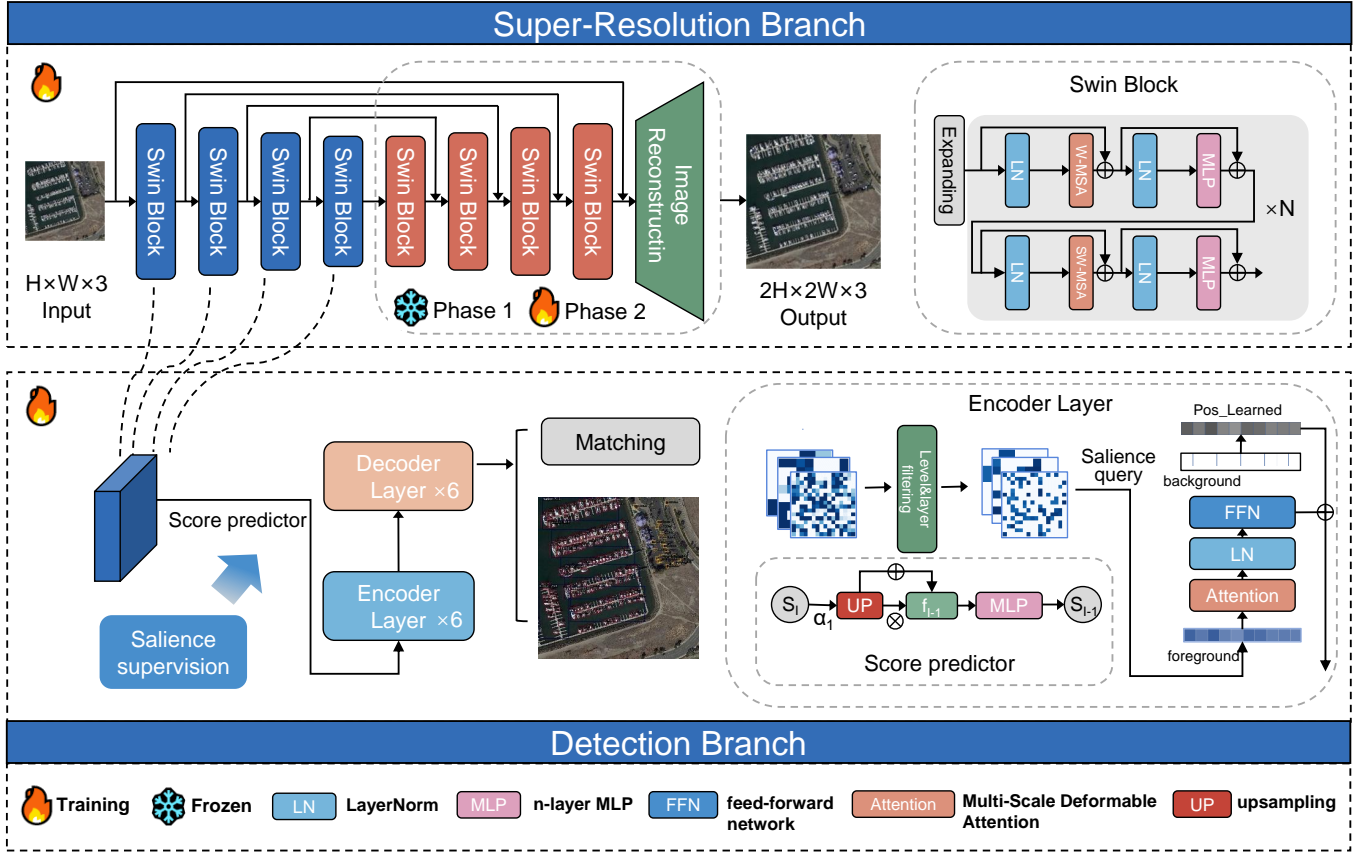


Fig. 2. **The framework pipeline of SDCoNet.** Our SDCoNet comprises two core branches: super-resolution and object detection, consisting of a shared encoder, a super-resolution decoder, a saliency-driven query filtering module, and an object detection encoder-decoder; in the first phase, the SR branch is frozen to update the object detection network, and in the second phase, dual-branch collaborative training is initiated.

encoder processes it through four progressive stages to generate a multi-scale feature pyramid. Specifically, at stage s ($s \in \{1, 2, 3, 4\}$), the encoder outputs feature maps $\mathbf{F}_s \in \mathbb{R}^{H_s \times W_s \times C_s}$, where the spatial resolution is downsampled by a factor of 2^{s+1} relative to the input image, and the channel dimensions are $C_1 = 96$, $C_2 = 192$, $C_3 = 384$, and $C_4 = 768$, respectively. The progressive feature extraction process can be formulated as:

$$\mathbf{F}_s = \text{SwinBlock}_s(\mathbf{F}_{s-1}), \quad s \in \{1, 2, 3, 4\}, \quad (1)$$

where $\mathbf{F}_0 = \mathbf{I}_{\text{LR}}$ represents the input image, and $\text{SwinBlock}_s(\cdot)$ denotes the s -th stage Swin block that consists of patch merging operations followed by stacked Swin Transformer layers. During training, the encoder parameters θ_{enc} simultaneously receive backpropagated gradients from both the SR reconstruction loss \mathcal{L}_{SR} and the detection losses (\mathcal{L}_{cls} , $\mathcal{L}_{\text{bbox}}$, $\mathcal{L}_{\text{giou}}$, \mathcal{L}_{sa}). The detailed formulation and optimization strategy for these loss functions are presented in Section III-E.

C. Super-Resolution Network Branch

The super-resolution decoder follows a hierarchical reconstruction design, integrating the progressive upsampling path of U-Net [50] with the feature modeling capabilities of Swin Transformer. To avoid notation ambiguity in subsequent formulations, we denote the input feature to a specific module

as \mathbf{Z}_{in} . The decoder consists of cascaded Patch Expanding modules and residual Swin Blocks. The Patch Expanding module restores spatial resolution via deconvolution and reshapes the feature dimensions to achieve granular recovery:

$$\mathbf{Z}_{\text{expand}} = \mathcal{R}_{\text{out}} \left(\text{TransConv} \left(\text{LN} \left(\mathcal{R}_{\text{in}}(\mathbf{Z}_{in}) \right) \right) \right), \quad (2)$$

where \mathbf{Z}_{in} represents the input feature map from the preceding level, and $\mathbf{Z}_{\text{expand}}$ is the upsampled output feature. $\mathcal{R}_{\text{in}}(\cdot)$ rearranges the input tensor from the spatial layout to a sequence format compatible with the transposed convolution. $\text{LN}(\cdot)$ denotes layer normalization applied along the channel dimension. $\text{TransConv}(\cdot)$ represents a transposed convolution with stride 2, which doubles the spatial resolution. Finally, $\mathcal{R}_{\text{out}}(\cdot)$ restores the expanded feature tensor back to the standard spatial layout for subsequent Swin Blocks.

To enhance feature representation, each Swin Transformer block employs a residual structure that encapsulates the window-based multi-head self-attention (Attn) and the multi-layer perceptron (MLP). The processing flow for a feature token sequence \mathbf{T}_{in} is defined as:

$$\mathbf{T}_{\text{out}} = \mathbf{T}_{in} + \text{MLP} \left(\text{LN} \left(\mathbf{T}_{in} + \text{Attn} \left(\text{LN} \left(\mathbf{T}_{in} \right) \right) \right) \right). \quad (3)$$

After progressively upsampling through multiple stages, the decoder produces the final decoded feature map \mathbf{F}_{dec} . The image reconstruction module then maps these deep features to the image domain. It utilizes lightweight convolutions combined with LeakyReLU (σ) for non-linear mapping and a PixelShuffle layer for upsampling. The final high-resolution output I_{SR} is obtained by:

$$I_{SR} = \text{Conv}(\text{PixelShuffle}(\sigma(\text{Conv}(\mathbf{F}_{\text{dec}})))), \quad (4)$$

where \mathbf{F}_{dec} denotes the final output features of the decoder. This structure effectively restores high-frequency details essential for identifying small objects in remote sensing imagery.

D. Saliency Map-Driven Query Token Selection

While DINO excels in denoising training and convergence speed, its standard DETR-based architecture processes all feature tokens indiscriminately. In remote sensing scenarios dominated by vast background areas and sparse small objects, this global attention mechanism introduces significant computational redundancy and background noise. To address this, we propose a saliency-driven hierarchical query token selection strategy. This mechanism acts as a spatial attention prior, guiding the swin transformer to focus its encoding resources solely on regions with high object probability.

The extracted shared multi-scale features are represented as $\{\mathbf{F}_l\}_{l=1}^L$, where \mathbf{F}_l represents the feature map of the l -th layer, with different spatial resolutions and channel numbers. They contain rich semantic information to support multi-size object detection.

1) *Saliency Score Prediction*: To operationalize the concept of spatial importance, we engineer a lightweight prediction module that estimates a saliency map from the feature pyramid. Recognizing that saliency relies on both local contrast and global context, we process the input features by splitting them along the channel dimension. The local branch preserves spatial detail, while the global branch undergoes global average pooling and broadcasting to capture scene-level context. These are concatenated and fused through a dimensionality-reducing MLP to produce a single-channel saliency score map S_l . The prediction process is defined as:

$$S_l = \text{MLP}_2(\mathcal{F}_{\text{fuse}}(\text{MLP}_1(\mathbf{F}_l))), \quad (5)$$

where $\mathcal{F}_{\text{fuse}}(\cdot)$ denotes the feature fusion operation that concatenates the local branch features $\mathbf{F}_{\text{local}}$ and the globally pooled-and-broadcasted features $\mathbf{F}_{\text{global}}$ along the channel dimension.

To ensure multiscale consistency, we implement a top-down propagation pathway. Saliency priors from coarse, high-level features are upsampled and fused with finer, low-level predictions. For the $l-1$ -th layer, the refined saliency map is:

$$S_{l-1} = \alpha \cdot \text{UP}(S_l) + \text{Saliency}(\mathbf{F}_{l-1}), \quad (6)$$

where α is a learnable modulation coefficient that dynamically weights the contribution of high-level semantics.

2) *Saliency Confidence Calculation Based on Relative Distance*: Merely predicting a binary foreground/background mask is insufficient for dense small object detection, as it lacks gradient information regarding object centrality. Therefore, we propose a scale-agnostic saliency confidence metric based on relative geometric positioning. This serves as a soft supervisory signal that measures the spatial alignment between a Query position (i, j) and the ground truth.

For a query located at (i, j) in the l -th feature map, mapped to global coordinates via Eq. 7, its confidence $C_l^{(i,j)}$ is modeled using a Gaussian decay function:

$$C_l^{(i,j)} = \begin{cases} \exp\left(-\frac{\Delta x^2 + \Delta y^2}{2\sigma^2}\right), & \text{if } (i, j) \in B_{GT} \\ 0, & \text{otherwise,} \end{cases} \quad (7)$$

where $\Delta x, \Delta y$ denote the offsets from the object center. Unlike discrete labels, this continuous Gaussian distribution provides smooth, distance-sensitive supervision. It naturally handles scale variations and provides stronger gradients for queries closer to the object center, significantly improving training stability for small targets.

3) *Hierarchical Query Filtering and Refinement*: Leveraging the predicted saliency scores, we implement a hierarchical query filtering mechanism to optimize the computational budget allocated to the Transformer encoder. As introduced in the motivation, processing the entirety of high-resolution remote sensing features is redundant. Therefore, we dynamically select the top $\beta_t \gamma_l N$ queries based on their saliency ranking to form the active set Φ_t , while masking the rest:

$$q_i = \begin{cases} \mathcal{A}(q_i + \text{pos}_i, q), & q_i \in \Phi_t, \\ q_i, & \text{otherwise,} \end{cases} \quad (8)$$

where β_t denotes the pyramid-level filtering ratio, which controls the number of queries retained across different feature scales, with values set to $(0.6, 0.8, 1.0, 1.0)$; and γ_l represents the Transformer layer-wise filtering ratio, indicating the proportion of queries involved in computation at layer l , with values $(1.0, 0.8, 0.6, 0.6, 0.4, 0.2)$. The filtering strength progressively increases as the network depth grows. Both β_t and γ_l take values within $(0, 1]$ and jointly determine the model's effective query budget.

By focusing Deformable Attention $\mathcal{A}(\cdot)$ only on Φ_t , the computational complexity is reduced from $O(NHK)$ to $O(\beta_t \gamma_l NHK)$. To prevent semantic collapse in the masked regions, we introduce a learnable background embedding $\mathbf{B}_{i,j} = \text{Concat}(\mathbf{R}_i, \mathbf{C}_j)$ added to the unselected queries. This strategy preserves consistent semantic priors for background regions while directing computation toward salient small objects, achieving a balance between detection accuracy and inference efficiency.

E. Model Optimization

Optimizing a joint SR-detection framework is challenging due to potential gradient conflicts between pixel-wise reconstruction and object-level recognition. We propose a detection-prioritized gradient routing strategy with a two-stage training

Algorithm 1 Detection-Prioritized Two-Stage Optimization

Input: Training set $\mathcal{D} = \{(x_n, y_n)\}_{n=1}^N$; shared multi-level feature encoder parameters θ_{feat} ; detection Transformer encoder-decoder and head parameters θ_{det} ; SR decoder parameters θ_{sr} ; Stage-One learning rates $\eta_{\text{feat}}^{(1)}, \eta_{\text{det}}^{(1)}$; Stage-Two learning rates $\eta_{\text{feat}}^{(2)}, \eta_{\text{det}}^{(2)}, \eta_{\text{sr}}^{(2)}$; scaling factor ρ ; detection pretraining epochs T_{det} ; total epochs T_{tot} .

Output: Optimized parameters $\theta_{\text{feat}}, \theta_{\text{det}}, \theta_{\text{sr}}$.

1: // **Stage One: Semantic Stabilization**

2: Set `requires_grad`(θ_{sr}) \leftarrow False

3: **for** $t = 1$ to T_{det} **do**

4: Sample mini-batch $\mathcal{B} \subset \mathcal{D}$

5: Construct low-resolution inputs and forward through shared encoder and detection Transformer encoder-decoder

6: Compute $\mathcal{L}_{\text{cls}}, \mathcal{L}_{\text{bbox}}, \mathcal{L}_{\text{giou}}, \mathcal{L}_{\text{sa}}$ on \mathcal{B}

7: $\mathcal{L}_{\text{stage1}} \leftarrow \beta_{\text{cls}}\mathcal{L}_{\text{cls}} + \beta_{\text{bbox}}\mathcal{L}_{\text{bbox}} + \beta_{\text{giou}}\mathcal{L}_{\text{giou}} + \beta_{\text{sa}}\mathcal{L}_{\text{sa}}$

8: Update θ_{feat} with $\eta_{\text{feat}}^{(1)}$ and θ_{det} with $\eta_{\text{det}}^{(1)}$ by back-propagating $\mathcal{L}_{\text{stage1}}$

9: **end for**

10: // **Stage Two: Collaborative Refinement**

11: Set `requires_grad`(θ_{sr}) \leftarrow True

12: Set $\eta_{\text{sr}}^{(2)} \leftarrow \rho \cdot \eta_{\text{det}}^{(2)}$, with $\rho < 1$

13: **for** $t = T_{\text{det}} + 1$ to T_{tot} **do**

14: Sample mini-batch $\mathcal{B} \subset \mathcal{D}$

15: Forward through shared encoder, detection Transformer encoder-decoder and SR decoder

16: Compute $\mathcal{L}_{\text{cls}}, \mathcal{L}_{\text{bbox}}, \mathcal{L}_{\text{giou}}, \mathcal{L}_{\text{sa}}, \mathcal{L}_{\text{sr}}$ on \mathcal{B}

17: $\mathcal{L}_{\text{stage2}} \leftarrow \beta_{\text{sr}}\mathcal{L}_{\text{sr}} + \beta_{\text{cls}}\mathcal{L}_{\text{cls}} + \beta_{\text{bbox}}\mathcal{L}_{\text{bbox}} + \beta_{\text{giou}}\mathcal{L}_{\text{giou}} + \beta_{\text{sa}}\mathcal{L}_{\text{sa}}$

18: Update θ_{feat} with $\eta_{\text{feat}}^{(2)}$, θ_{det} with $\eta_{\text{det}}^{(2)}$, and θ_{sr} with $\eta_{\text{sr}}^{(2)}$ by back-propagating $\mathcal{L}_{\text{stage2}}$

19: **end for**

schedule. Let θ_{feat} , θ_{det} , and θ_{sr} represent the shared encoder, detection head, and SR branch parameters, respectively.

Stage One: The SR branch is frozen, and only θ_{feat} and θ_{det} are updated using detection-related losses: classification loss \mathcal{L}_{cls} , bounding box loss $\mathcal{L}_{\text{bbox}}$, GIoU loss $\mathcal{L}_{\text{giou}}$, and saliency constraint loss \mathcal{L}_{sa} (Sigmoid Focal Loss for hard-to-detect small objects). This anchors the encoder in a detection-oriented semantic space.

Stage Two: θ_{sr} is unfrozen for joint optimization with task-specific learning rates:

$$\eta_{\text{feat}}^{(2)}, \eta_{\text{det}}^{(2)}, \eta_{\text{sr}}^{(2)} = \rho \eta_{\text{det}}^{(2)}, \quad 0 < \rho < 1, \quad (9)$$

where $\eta_{\text{feat}}^{(2)}$, $\eta_{\text{det}}^{(2)}$, and $\eta_{\text{sr}}^{(2)}$ denote the learning rates for the shared encoder, detection head, and SR branch, respectively. The scaling factor $\rho \in (0, 1)$ ensures conservative SR updates, allowing detection semantics to dominate while SR provides complementary pixel-level refinement.

Overall Loss Functions:

For Stage One:

$$\mathcal{L}_{\text{stage1}} = \beta_{\text{cls}}\mathcal{L}_{\text{cls}} + \beta_{\text{bbox}}\mathcal{L}_{\text{bbox}} + \beta_{\text{giou}}\mathcal{L}_{\text{giou}} + \beta_{\text{sa}}\mathcal{L}_{\text{sa}}, \quad (10)$$

where β_{cls} , β_{bbox} , β_{giou} , and β_{sa} are weighting coefficients for each loss term.

For Stage Two:

$$\mathcal{L}_{\text{stage2}} = \beta_{\text{sr}}\mathcal{L}_{\text{sr}} + \beta_{\text{cls}}\mathcal{L}_{\text{cls}} + \beta_{\text{bbox}}\mathcal{L}_{\text{bbox}} + \beta_{\text{giou}}\mathcal{L}_{\text{giou}} + \beta_{\text{sa}}\mathcal{L}_{\text{sa}}, \quad (11)$$

where β_{sr} controls the SR reconstruction loss contribution. The overall training process is summarized in Algorithm 1.

IV. EXPERIMENTS AND ANALYSIS*A. Implementation Details*

1) Datasets: To comprehensively evaluate the proposed method, we conduct experiments on three benchmark remote sensing datasets: NWPU VHR-10 [21], DOTAv1.5 [22] and HRSSD [23]. Note that our method focuses on horizontal bounding box (HBB) detection. A standard preprocessing step, the sliding-window cropping strategy, is adopted to meet the network input requirements and minimize the potential loss of information caused by direct resizing.

DOTAv1.5 Dataset [22]: The DOTAv1.5 dataset contains large-scale high-resolution remote sensing images with sizes reaching up to 4000×4000 pixels. To facilitate processing, these images are cropped into 1024×1024 patches with a 200-pixel overlap to ensure that objects near patch boundaries remain intact. For images smaller than 1024×1024 pixels, zero-padding is applied. The resulting DOTAv1.5-Split dataset consists of 11,828 training images and 4,055 testing images.

NWPU VHR-10 Dataset [21]: The NWPU VHR-10 dataset is a collection of high-resolution remote sensing images with a focus on various object categories, including vehicles and buildings. For this dataset, we apply a similar preprocessing strategy by cropping the original images into 512×512 patches with a 100-pixel overlap. This results in a total of 3,631 images in the NWPU VHR-10-Split dataset.

HRSSD Dataset [23]: The HRSSD dataset includes high-resolution remote sensing images that cover a wide range of small-object categories. Similar to DOTAv1.5, these images are cropped into 1024×1024 patches with a 200-pixel overlap, yielding 53,056 images in the HRSSD-Split dataset.

Representative examples for each dataset are shown on the left side (High-Resolution) of Fig. 3, and category distributions are illustrated in Fig. 4. Detailed statistics are summarized in Table I.

TABLE I
DATASET STATISTICAL INFORMATION

Dataset	Categories	Images	Total objects
DOTAv1.5-Split [22]	16	15883	408390
NWPU VHR-10-Split [21]	10	3631	10389
HRSSD-Split [23]	13	53056	86817

2) Training and Optimization Settings: In the super-resolution (SR) setup, we simulate low-quality remote sensing conditions to rigorously assess both reconstruction and detection performance. The cropped 1024×1024 and 512×512 patches are treated as High-Resolution (HR) ground truth. Each HR image is downsampled by a factor of 2 using bicubic interpolation to generate the corresponding Low-Resolution (LR) input, as shown in Fig. 3. During training, the network

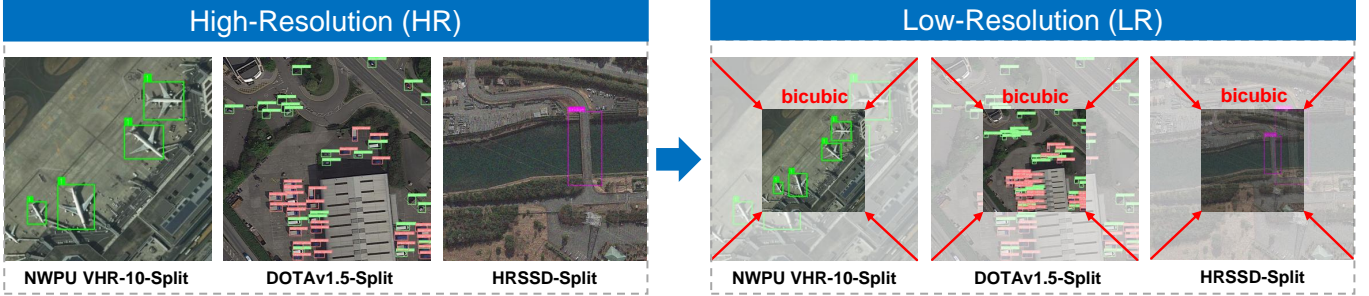


Fig. 3. Example images from the DOTA1.5-Split [22], NWPU VHR-10-Split [21], and HRSSD-Split [23] datasets. The left side shows high-resolution images from these datasets, while the right side presents the corresponding low-resolution images generated by bicubic downsampling.

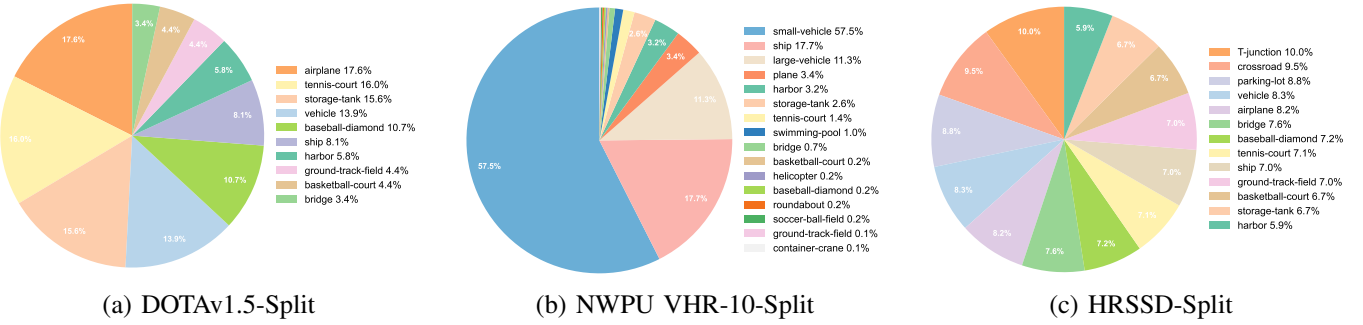


Fig. 4. Category distribution of the benchmark datasets. The pie charts show the class proportions of the DOTA1.5-Split [22], NWPU VHR-10-Split [21], and HRSSD-Split [23] datasets, which contain a large number of small-object categories such as storage-tank, small-vehicle, bridge, and ship.

only receives these LR images (512×512 or 256×256), which forces the model to recover fine details and detect objects from significantly degraded visual evidence.

The network is implemented in PyTorch and trained on a single NVIDIA RTX 3090 GPU with a batch size of 2. The model is trained using the AdamW optimizer with an initial learning rate of 1×10^{-4} and a weight decay of 1×10^{-4} , equipped with gradient clipping (max_norm=0.1) and a 0.1x learning-rate multiplier for the backbone. The learning rate follows a multi-step decay schedule (MultiStepLR), where it is reduced by a factor of 0.1 according to predefined milestones within an epoch-based training loop. A two-stage training strategy is adopted, in which the detection network is trained for the first 16 epochs and the entire model is subsequently optimized jointly for the remaining epochs under the same learning-rate policy. Throughout training and testing, the input resolution is kept fixed, and no additional data augmentation is used in order to provide a controlled and reproducible evaluation protocol. Following DINO, we report mean Average Precision (AP) under multiple IoU thresholds as the primary metric to quantify detection performance.

B. Comparison with State-of-the-Art Models

To evaluate the performance of SDCoNet, we compare it with a set of representative state-of-the-art object detectors, taking DINO as the baseline. The quantitative results on NWPU VHR-10-Split [21], DOTA1.5-Split [22], and HRSSD-Split [23] are summarized in Tables II–IV, where all methods are retrained under identical experimental settings.

As shown in Tables II–IV, we compare SDCoNet against a comprehensive set of methods, including Faster R-CNN [14], RetinaNet [51], Cascade R-CNN [52], YOLOX-s [53], Sparse R-CNN [54], DAB-DETR [11], DN-DETR [12], Deformable DETR [13], DINO [48], SR4IR [10], EESRGAN [9], SuperYOLO [56], FSANet [55], FFCA-YOLO [16], and LEGNet-T [43]. These baselines encompass CNN-based one-stage and two-stage detectors, Transformer-based DETR variants, a two-stage serial SR-detection pipeline (SR4IR), as well as methods specifically designed for remote sensing object detection (EESRGAN, SuperYOLO, FSANet, FFCA-YOLO, and LEGNet-T). Notably, LEGNet-T is a lightweight yet effective backbone proposed in 2025 for remote sensing object detection. We integrate it with Faster R-CNN and adapt it to horizontal bounding box detection for evaluation. For SuperYOLO, which is originally a multimodal fusion-based detector, we conduct experiments using only RGB images for fair comparison. SDCoNet consistently outperforms all these competitors across all three benchmarks, particularly in terms of overall accuracy and small-object detection capabilities.

Relative to the strongest baseline, Swin-T DINO [48], SDCoNet demonstrates significant performance advantages. Specifically, on the NWPU VHR-10-Split, our method achieves absolute gains of 7.0%, 0.5%, and 16.2% in AP, AP₅₀, and AP_s, respectively. Similarly, improvements of 1.7%, 1.5%, and 5.8% on DOTA1.5-Split, and 1.0%, 1.1%, and 5.6% on HRSSD-Split are observed. Notably, the substantial boost in AP_s validates that the proposed saliency-driven SR-detection collaboration effectively generates discriminative

TABLE II

PERFORMANCE COMPARISON OF SDCoNET WITH REPRESENTATIVE OBJECT DETECTORS ON THE NWPU VHR-10-SPLIT DATASET. ALL DETECTORS ARE TRAINED AND EVALUATED ON LOW-RESOLUTION IMAGES OBTAINED BY $2 \times$ BICUBIC DOWNSAMPLING OF THE ORIGINAL HIGH-RESOLUTION INPUTS. UNDERLINED NUMBERS DENOTE THE SECOND-BEST RESULTS, WHILE BOLDFACE INDICATES THE BEST PERFORMANCE IN EACH COLUMN

Type	Method	Backbone	AP	AP ₅₀	AP ₇₅	AP _s	AP _m	AP _l
General Object Detectors	Faster RCNN [14]	ResNet50	0.729	0.964	0.885	0.326	0.717	0.795
	RetinaNet [51]	ResNet50	0.610	0.899	0.705	0.173	0.563	0.745
	Cascade R-CNN [52]	ResNet50	0.627	0.910	0.738	0.159	0.601	0.696
	YOLOX-s [53]	CSPDarknet	0.766	0.964	0.892	0.450	0.750	0.802
	Sparse R-CNN [54]	ResNet50	0.381	0.678	0.356	0.025	0.316	0.617
	SR4IR [10]	MobileNet-V3	0.743	0.967	0.878	0.308	0.725	<u>0.844</u>
	DAB-DETR [11]	ResNet50	0.656	0.935	0.756	0.342	0.609	0.791
	DN-DETR [12]	ResNet50	0.681	0.936	0.782	0.299	0.652	0.800
	DINO [48]	ResNet50	<u>0.793</u>	0.980	<u>0.933</u>	0.534	<u>0.769</u>	0.832
	Deformable-DETR [13]	Swin-T	<u>0.345</u>	0.620	<u>0.344</u>	0.048	0.296	0.464
	DINO (Baseline) [48]	Swin-T	0.766	<u>0.986</u>	0.911	0.487	0.744	0.830
Remote Sensing Object Detectors	EESRGAN [9]	ResNet50	0.749	0.971	0.891	0.448	0.724	0.802
	FSANet [55]	Swin-T	0.671	0.956	0.791	0.306	0.649	0.754
	SuperYOLO (RGB) [56]	CSPDarknet	0.700	0.868	0.825	<u>0.554</u>	0.704	0.773
	FFCA-YOLO [16]	CSPDarknet	0.689	0.946	0.836	0.427	0.688	0.778
	LEGNet-T (Faster RCNN) [43]	LEGNet-T	0.788	0.979	0.921	0.449	<u>0.769</u>	0.841
	SDCoNet (Ours)	Swin-T	0.836	0.991	0.954	0.649	0.816	0.890

TABLE III
COMPARISONS WITH DIFFERENT OBJECT DETECTORS ON THE DOTAV1.5-SPLIT DATASET

Type	Method	Backbone	AP	AP ₅₀	AP ₇₅	AP _s	AP _m	AP _l
General Object Detectors	Faster RCNN [14]	ResNet50	0.303	0.487	0.327	0.093	0.338	0.434
	RetinaNet [51]	ResNet50	0.243	0.413	0.247	0.021	0.239	0.390
	Cascade R-CNN [52]	ResNet50	0.265	0.434	0.275	0.065	0.279	0.388
	YOLOX-s [53]	CSPDarknet	0.269	0.498	0.277	0.119	0.292	0.347
	Sparse R-CNN [54]	ResNet50	0.266	0.446	0.279	0.060	0.263	0.422
	SR4IR [10]	MobileNet-V3	0.329	0.511	0.340	0.147	0.358	0.495
	DAB-DETR [11]	ResNet50	0.233	0.440	0.215	0.035	0.211	0.394
	DN-DETR [12]	ResNet50	0.274	0.462	0.254	0.030	0.289	0.425
	DINO [48]	ResNet50	0.367	0.597	0.397	0.160	0.394	0.506
	Deformable-DETR [13]	Swin-T	0.248	0.464	0.229	0.044	0.256	0.434
	DINO (Baseline) [48]	Swin-T	<u>0.402</u>	<u>0.659</u>	<u>0.427</u>	0.192	<u>0.434</u>	<u>0.540</u>
Remote Sensing Object Detectors	EESRGAN [9]	ResNet50	0.314	0.512	0.342	0.160	0.360	0.481
	FSANet [55]	Swin-T	0.283	<u>0.557</u>	0.271	0.103	0.312	0.384
	SuperYOLO (RGB) [56]	CSPDarknet	0.307	0.495	0.397	0.191	0.335	0.429
	FFCA-YOLO [16]	CSPDarknet	0.399	0.642	0.425	<u>0.221</u>	0.425	0.470
	LEGNet-T (Faster RCNN) [43]	LEGNet-T	0.316	0.508	0.343	0.084	0.361	0.434
	SDCoNet (Ours)	Swin-T	0.419	0.674	0.455	0.250	0.451	0.562

features for dense small objects amidst cluttered backgrounds, while simultaneously securing robust overall detection accuracy. To further underscore the superiority of this collaborative framework beyond mere accuracy, we present an analysis of the accuracy–efficiency trade-off compared to two-stage serial SR–detection pipelines in Section IV-F. To provide a more fine-grained evaluation, Fig. 5 presents the per-category AP comparison on the NWPU VHR-10-Split dataset. As illustrated, SDCoNet achieves substantial AP improvements for small-object categories such as storage-tank and vehicle

when compared against the baseline DINO, the classic Faster R-CNN, as well as existing state-of-the-art approaches. This category-level analysis further corroborates that the proposed saliency-driven collaborative mechanism effectively enhances the discriminability of challenging small targets that are otherwise prone to missed detections.

Visualization results in Fig. 6 are consistent with the quantitative findings. On NWPU VHR-10-Split, SDCoNet reliably detects densely arranged tennis and basketball courts with fewer missed and spurious detections than Faster R-

TABLE IV
COMPARISONS WITH DIFFERENT OBJECT DETECTORS ON THE HRSSD-SPLIT DATASET

Type	Method	Backbone	AP	AP ₅₀	AP ₇₅	AP _s	AP _m	AP _l
General Object Detectors	Faster RCNN [14]	ResNet50	0.584	0.858	0.671	0.115	0.509	0.592
	RetinaNet [51]	ResNet50	0.520	0.812	0.566	0.052	0.410	0.533
	Cascade R-CNN [52]	ResNet50	0.529	0.814	0.581	0.058	0.430	0.535
	YOLOX-s [53]	CSPDarknet	0.586	0.834	0.664	0.185	0.441	0.599
	Sparse R-CNN [54]	ResNet50	0.340	0.552	0.361	0.004	0.223	0.385
	SR4IR [10]	MobileNet-V3	0.637	0.871	0.702	0.204	0.528	0.665
	DAB-DETR [11]	ResNet50	0.585	0.868	0.655	0.126	0.430	0.605
	DN-DETR [12]	ResNet50	0.604	0.870	0.687	0.244	0.486	0.621
	DINO [48]	ResNet50	0.663	0.893	0.767	0.356	0.579	0.648
	Deformable-DETR [13]	Swin-T	0.302	0.541	0.337	0.035	0.219	0.374
	DINO (Baseline) [48]	Swin-T	0.691	0.926	0.806	0.315	0.591	0.681
Remote Sensing Object Detectors	EESRGAN [9]	ResNet50	0.612	0.870	0.693	0.187	0.508	0.595
	FSANet [55]	Swin-T	0.562	0.876	0.635	0.053	0.485	0.562
	SuperYOLO (RGB) [56]	CSPDarknet	0.581	0.883	0.694	0.263	0.494	0.587
	FFCA-YOLO [16]	CSPDarknet	0.622	0.893	0.713	0.099	0.543	0.616
	LEGNet-T (Faster RCNN) [43]	LEGNet-T	0.614	0.900	0.715	0.176	0.539	0.620
	SDCoNet (Ours)	Swin-T	0.701	0.937	0.820	0.371	0.619	0.680

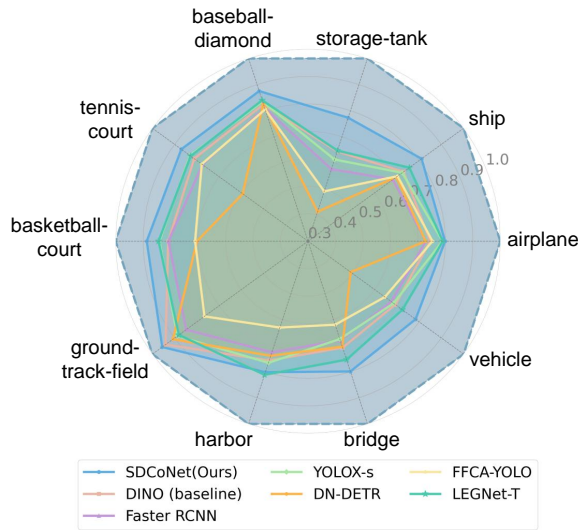


Fig. 5. Per-class detection performance on the NWPU VHR-10-Split dataset. The chart compares SDCoNet with representative CNN-based (Faster R-CNN, YOLOX-s, FFCA-YOLO, LEGNet-T) and Transformer-based (DINO, DN-DETR) detectors, showing consistent gains for small-object categories such as storage-tank and vehicle.

CNN, RetinaNet, Cascade R-CNN, YOLOX-s, Sparse R-CNN, Deformable DETR, and DINO. On DOTAv1.5-Split, SDCoNet better separates visually similar categories such as airplanes and helicopters, and recovers very small ships and vehicles in port scenes with higher recall and fewer false alarms. On HRSSD-Split, SDCoNet provides more precise localization of shore-side ships and bridge targets, avoiding the category confusion observed in DINO (e.g., misclassifying a road fork as a bridge). These qualitative comparisons demonstrate that the proposed saliency-driven multi-task collaborative mechanism effectively suppresses background clutter, improves coverage

of dense small objects, and enhances discrimination of easily confused categories in complex remote sensing scenes.

C. Ablation on the Super-Resolution Branch

To quantify the contribution of the proposed super-resolution (SR) branch to detection performance on low-quality remote sensing imagery, we conduct ablation studies on DOTAv1.5-Split and NWPU VHR-10-Split using Cascade R-CNN and DINO as representative CNN- and Transformer-based baselines. The corresponding results are reported in Table V.

Across both benchmarks and both baselines, enabling the SR branch (*SR Branch* marked with a check mark in Table V) consistently improves overall detection accuracy and, more importantly, substantially boosts small-object performance. For instance, on NWPU VHR-10-Split, equipping Cascade R-CNN and DINO with the SR branch yields higher AP and a clear increase in the small-object metric AP_s compared with their respective baselines. A similar trend is observed on DOTAv1.5-Split, where the SR-augmented variants provide stronger responses to small targets while preserving or slightly improving medium and large object detection.

Unlike traditional serial enhancement methods, our collaborative strategy leverages a shared encoder, allowing the object detector to benefit from the high-frequency spatial details recovered by the SR task. This implicitly forces the backbone to learn more robust representations that are resilient to blur and noise. Crucially, since the SR head is discarded during inference, these improvements in representation quality are achieved without incurring any additional computational cost during the deployment phase.

To investigate the impact of the Super-Resolution (SR) branch on the detector's representational capacity, we visualize and compare the intermediate feature maps from the four stages of the shared encoder. Specifically, we use the DINO

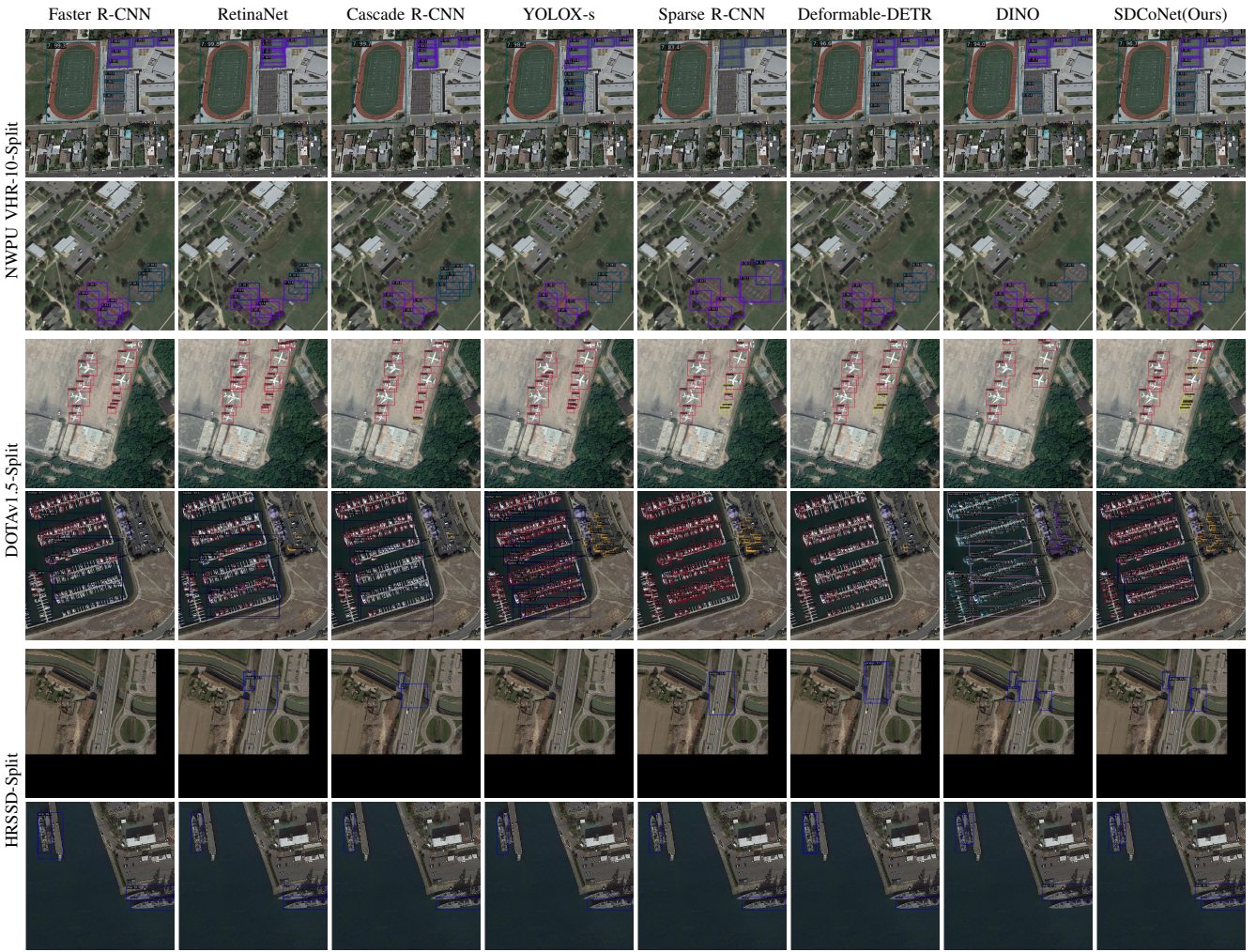


Fig. 6. **Qualitative detection results of the proposed SDCoNet compared with representative state-of-the-art detectors.** From left to right, the columns correspond to Faster R-CNN, RetinaNet, Cascade R-CNN, YOLOX-s, Sparse R-CNN, Deformable DETR, DINO, and SDCoNet. From top to bottom, the rows show visualization results on the NWPU VHR-10-Split [21], DOTAv1.5-Split [22], and HRSSD-Split [23] datasets, respectively.

model as a baseline and contrast its activation maps with those of the SR-augmented model. As shown in Fig. 7, the inclusion of the SR branch significantly alters the feature response patterns across different hierarchical layers, demonstrating the effectiveness of our multi-task collaborative design.

In the shallow layers (Stage 1 and Stage 2), the baseline model’s feature maps often show strong background noise interference and blurred boundaries, which hinder small object detection. For Stage 1, there is no noticeable change, but in Stage 2, the SR-augmented model exhibits clearer pixel-level delineation, with a more distinct separation between foreground and background regions. As the network progresses into deeper layers (Stage 3 and Stage 4), the enhanced structural representation translates into stronger semantic discriminability. The baseline model generates more diffuse activations, which occasionally fail to highlight small targets (such as airplanes) in complex airport environments. In contrast, the SR-augmented model shows more concentrated semantic activations, with the feature responses tightly focused on the specific location of the airplane, effectively suppressing background clutter. This indicates that the SR branch optimizes the

alignment of deep semantic features, improving the accuracy of object localization.

D. Ablation on Saliency Guidance

We further explore the necessity of Saliency Prior Maps in guiding the attention of Query Tokens. Table VI presents a comparative analysis on the NWPU VHR-10-Split dataset across four configurations: the baseline DINO, DINO with saliency (DINO-Saliency), DINO with SR (DINO-SR Branch), and our full SDCoNet. While the SR branch alone improves performance, the integration of saliency guidance (SDCoNet) further pushes the AP to 0.836, surpassing the DINO-SR Branch by 2.0 percentage points.

This significant boost validates that the saliency maps effectively act as a spatial attention prior, guiding the limited number of Query Tokens to focus on information-rich regions rather than background clutter. This mechanism is particularly beneficial in multi-task learning, as it mitigates the potential noise introduced by task coupling and ensures that the SR-enhanced features are correctly attended to by the detection head.

TABLE V

EFFECT OF THE SUPER-RESOLUTION (SR) BRANCH ON DETECTION PERFORMANCE. “SR BRANCH” INDICATES WHETHER THE SR BRANCH IS ENABLED. VALUES SHOWN IN PARENTHESSES (IN BLUE) REPRESENT THE PERFORMANCE IMPROVEMENTS RELATIVE TO THE BASELINE

Dataset	Method	SR Branch	AP	AP ₅₀	AP _s	AP _m	AP _l
NWPU VHR-10-Split [21]	Cascade R-CNN [52]	✓	0.627 0.644 (+0.017)	0.910 0.913 (+0.003)	0.159 0.268 (+0.109)	0.601 0.647 (+0.046)	0.696 0.721 (+0.025)
	DINO [48]	✓	0.766 0.816 (+0.050)	0.986 0.990 (+0.004)	0.487 0.552 (+0.065)	0.744 0.794 (+0.050)	0.830 0.886 (+0.056)
DOTAV1.5-Split [22]	Cascade R-CNN [52]	✓	0.265 0.277 (+0.012)	0.434 0.440 (+0.006)	0.065 0.143 (+0.078)	0.279 0.299 (+0.020)	0.388 0.406 (+0.018)
	DINO [48]	✓	0.402 0.412 (+0.010)	0.659 0.663 (+0.004)	0.192 0.221 (+0.029)	0.434 0.445 (+0.011)	0.540 0.560 (+0.020)

TABLE VI

COMPARISON OF SALIENCY-DRIVEN AND BASELINE CONFIGURATIONS FOR OBJECT DETECTION PERFORMANCE

Method	Saliency	SR Branch	AP	AP ₅₀	AP ₇₅	AP _s	AP _m	AP _l
DINO(baseline) [48]			0.766	0.986	0.911	0.487	0.744	0.830
DINO-Saliency	✓		0.776	0.991	0.918	0.474	0.759	0.841
DINO-SR Branch		✓	<u>0.816</u>	<u>0.990</u>	<u>0.939</u>	<u>0.552</u>	<u>0.794</u>	<u>0.886</u>
SDCoNet (Ours)	✓	✓	0.836	0.991	0.954	0.649	0.816	0.890

TABLE VII

COMPARISON OF DIFFERENT FUSION STRATEGIES FOR THE MODULATION COEFFICIENT α

Setting	AP	AP ₅₀	AP ₇₅	AP _s	AP _m	AP _l
Remove α	0.825	<u>0.990</u>	0.961	0.645	<u>0.809</u>	0.871
Fixed α	0.831	<u>0.990</u>	0.956	0.648	0.807	0.880
Learnable α	0.836	0.991	0.954	0.649	0.816	0.890

TABLE VIII

COMPARISON WITH TWO-STAGE SR-DETECTION PIPELINES ON THE NWPU VHR-10-SPLIT DATASET

Method	AP	AP ₅₀	AP ₇₅	FPS	FLOPs
SR4IR [10]	0.745	0.967	0.878	11.1	65.80G
SDCoNet-Serial	0.766	0.990	0.893	10.8	88.22G
SDCoNet	0.836	0.991	0.954	18.6	16.94G

E. Analysis of Dynamic Modulation Mechanism

The modulation coefficient α (defined in Eq. 6) governs the intensity of saliency propagation. To determine the optimal fusion strategy, we compare three settings: removing α (equivalent to $\alpha = 1$), fixing $\alpha = 0.5$, and treating α as a learnable parameter. The results in Table VII clearly favor the learnable α setting. The learnable α setting achieves the highest AP of 0.836, outperforming the fixed constant setting (0.831) and the removal setting (0.825).

This superiority stems from the learnable parameter’s ability to adaptively regulate the injection of high-level semantic priors. Unlike a fixed coefficient that may lead to either inadequate background suppression or excessive smoothing of local details, a learnable α optimizes the intensity of this top-down modulation, ensuring an effective integration of coarse semantic context with fine spatial details.

F. Computational Efficiency Analysis

1) *Comparison with Two-Stage SR-detection Pipelines:* A critical limitation of traditional “SR-detection” serial pipelines is the objective misalignment, where super-resolution reconstruction may conflict with detection-oriented semantics. As demonstrated in Table VIII, we compare SDCoNet against a state-of-the-art serial method (SR4IR [10]) and a baseline

serial implementation (SDCoNet-Serial). The serial approach suffers from high computational redundancy (88.22G FLOPs) and suboptimal accuracy (0.766 AP). In contrast, our parallel, unified framework not only reduces the computational load to 16.94G FLOPs (a 5 \times reduction compared to the serial baseline) but also achieves a superior AP of 0.836. This confirms that collaborative optimization in a shared feature space is far more effective than sequential processing for low-quality inputs.

2) *Effect of Hierarchical Query Token Selection on Efficiency:* Finally, we analyze the impact of our hierarchical Query Token selection strategy on inference efficiency. Table IX presents an ablation where tokens are filtered at different stages. Retaining all tokens (“No hierarchical filtering”) results in high computational overhead (22.93G FLOPs) without yielding the best accuracy (0.824 AP), as redundant background tokens dilute the attention mechanism. By implementing our joint layer-wise and scale-level filtering, we reduce the FLOPs to 16.94G while simultaneously improving AP to 0.836. The joint mechanism essentially acts as a semantic filter, discarding approximately 60% of non-informative queries based on saliency rankings. This ensures that computational resources are concentrated exclusively on regions with high object probability, demonstrating an optimal balance between detection precision and model efficiency.

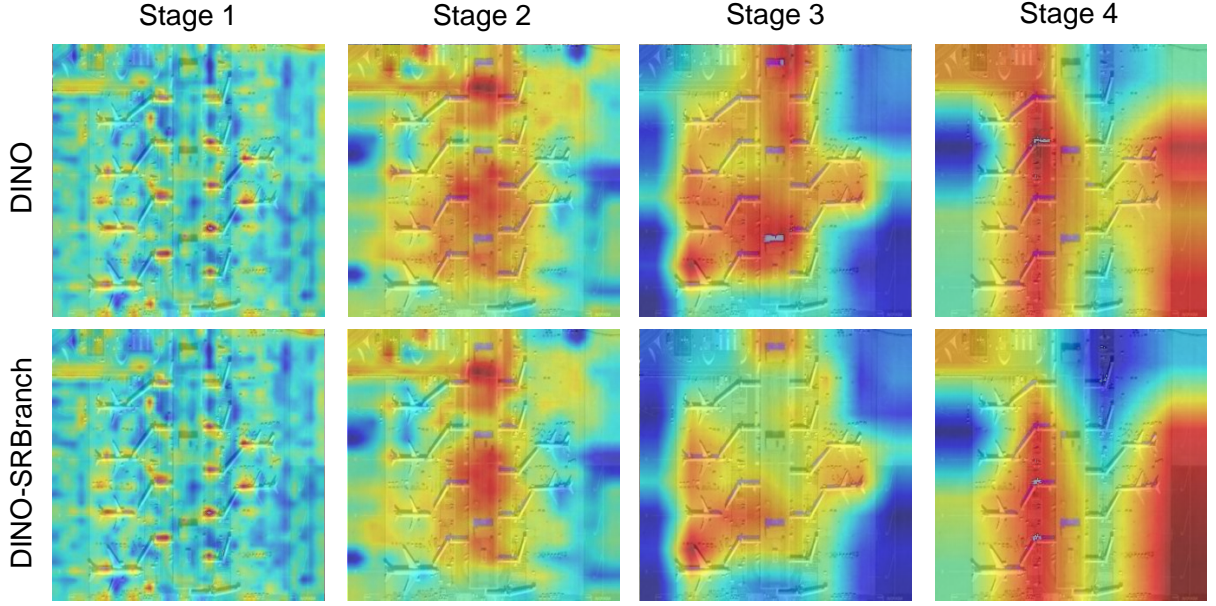


Fig. 7. **Visualization of intermediate feature maps for the baseline DINO and the SR-augmented DINO-SR Branch on the NWPU VHR-10-Split [21] dataset.** From left to right, the columns correspond to backbone stages 1–4; within each stage, the first rows show the activation maps of DINO, while the second rows show those of DINO-SR Branch.

TABLE IX
EFFICIENCY AND ACCURACY TRADE-OFFS UNDER DIFFERENT QUERY TOKEN FILTERING STRATEGIES

Setting	AP	AP ₅₀	AP ₇₅	FLOPs
No hierarchical filtering	0.824	0.990	0.955	22.93G
Layer-wise filtering	0.825	0.993	0.951	<u>18.97G</u>
Scale-level filtering	<u>0.829</u>	0.990	0.952	19.57G
Joint filtering	0.836	0.991	0.954	16.94G

V. CONCLUSION

In this paper, we propose SDCoNet, a saliency-driven collaborative framework designed to enhance small object detection in low-quality remote sensing imagery. By moving beyond the conventional serial paradigm, SDCoNet effectively mitigates the objective misalignment and spatial attention diffusion that typically plague multi-task pipelines. Our approach facilitates a semantically consistent interaction between super-resolution and detection through an implicit feature sharing paradigm, coupled with a gradient routing strategy that harmonizes disparate optimization signals. Furthermore, the introduced saliency-driven mechanism ensures that the model maintains focus on critical object regions, effectively filtering out task-irrelevant high-frequency noise. Experimental results demonstrate that SDCoNet significantly outperforms state-of-the-art methods on multiple datasets. While this work successfully narrows the gap between pixel-level reconstruction and semantic discrimination, future research will investigate more granular bidirectional guidance mechanisms and adaptive task-weighting schemes to further unlock the potential of multi-task synergy in complex Earth observation scenarios.

REFERENCES

- [1] M. Nikouei, B. Baroutian, S. Nabavi, F. Taraghi, A. Aghaei, A. Sajedi, and M. E. Moghaddam, “Small object detection: A comprehensive survey on challenges, techniques and real-world applications,” *Intelligent Systems with Applications*, vol. 27, p. 200561, 2025.
- [2] S. Gui, S. Song, R. Qin, and Y. Tang, “Remote sensing object detection in the deep learning era—a review,” *Remote Sensing*, vol. 16, p. 327, 2024.
- [3] H. Su, Y. Li, Y. Xu, X. Fu, and S. Liu, “A review of deep-learning-based super-resolution: From methods to applications,” *Pattern Recognition*, vol. 157, p. 110935, 2025.
- [4] D. C. Lepcha, B. Goyal, A. Dogra, and V. Goyal, “Image super-resolution: A comprehensive review, recent trends, challenges and applications,” *Information Fusion*, vol. 91, pp. 230–260, 2023.
- [5] Y. Wang, Z. Shao, T. Lu, X. Huang, J. Wang, Z. Zhang, and X. Zuo, “Lightweight remote sensing super-resolution with multi-scale graph attention network,” *Pattern Recognition*, vol. 160, p. 111178, 2025.
- [6] N. Alsaedi and B. Shah, “A novel hybrid deep learning approach for super-resolution and objects detection in remote sensing,” *Scientific Reports*, vol. 15, p. 1476, 2025.
- [7] M. Haris, G. Shakhnarovich, and N. Ukita, “Task-driven super resolution: Object detection in low-resolution images,” in *International Conference on Neural Information Processing*. Springer, 2021, pp. 387–395.
- [8] Y. Liu, Z. Xiong, Y. Yuan, and Q. Wang, “Distilling knowledge from super-resolution for efficient remote sensing salient object detection,” *IEEE Transactions on Geoscience and Remote Sensing*, vol. 61, pp. 1–16, 2023.
- [9] J. Rabbi, N. Ray, M. Schubert, S. Chowdhury, and D. Chao, “Small-object detection in remote sensing images with end-to-end edge-enhanced gan and object detector network,” *Remote Sensing*, vol. 12, no. 9, p. 1432, 2020.
- [10] J. Kim, J. Oh, and K. M. Lee, “Beyond image super-resolution for image recognition with task-driven perceptual loss,” in *Proceedings of the IEEE/CVF Conference on Computer Vision and Pattern Recognition*, 2024, pp. 2651–2661.
- [11] S. Liu, F. Li, H. Zhang, X. Yang, X. Qi, H. Su, J. Zhu, and L. Zhang, “Dab-detr: Dynamic anchor boxes are better queries for detr. arxiv 2022,” *arXiv preprint arXiv:2201.12329*.
- [12] F. Li, H. Zhang, S. Liu, J. Guo, L. M. Ni, and L. Zhang, “Dn-detr: Accelerate detr training by introducing query denoising,” in *Proceedings of the IEEE/CVF conference on computer vision and pattern recognition*, 2022, pp. 13 619–13 627.

[13] X. Zhu, W. Su, L. Lu, B. Li, X. Wang, and J. Dai, "Deformable detr: Deformable transformers for end-to-end object detection," *arXiv preprint arXiv:2010.04159*, 2020.

[14] S. Ren, K. He, R. Girshick, and J. Sun, "Faster r-cnn: Towards real-time object detection with region proposal networks," *IEEE transactions on pattern analysis and machine intelligence*, vol. 39, no. 6, pp. 1137–1149, 2017.

[15] J. Redmon and A. Farhadi, "Yolo9000: Better, faster, stronger," in *2017 IEEE Conference on Computer Vision and Pattern Recognition (CVPR)*, 2017, pp. 6517–6525.

[16] Y. Zhang, M. Ye, G. Zhu, Y. Liu, P. Guo, and J. Yan, "Ffca-yolo for small object detection in remote sensing images," *IEEE Transactions on Geoscience and Remote Sensing*, vol. 62, pp. 1–15, 2024.

[17] K. Jin, W. Du, M. Tang, W. Liang, K. Li, and A.-S. K. Pathan, "Lsodnet: A lightweight and efficient detector for small object detection in remote sensing images," *IEEE Journal of Selected Topics in Applied Earth Observations and Remote Sensing*, vol. 18, pp. 24 816–24 828, 2025.

[18] Y. Kong, X. Shang, and S. Jia, "Drone-detr: Efficient small object detection for remote sensing image using enhanced rt-detr model," *Sensors*, vol. 24, no. 17, p. 5496, 2024.

[19] J. Li *et al.*, "Rs-detr: An improved remote sensing object detection model based on rt-detr," *Applied Sciences*, vol. 14, no. 22, p. 10331, 2024.

[20] A. Miri Rekavandi, S. Rashidi, F. Boussaid, S. Hoefs, E. Akbas, and M. Bennamoun, "Transformers in small object detection: A benchmark and survey of state-of-the-art," *ACM Computing Surveys*, vol. 57, no. 4, pp. 1–37, 2024.

[21] G. Cheng, P. Zhou, and J. Han, "Learning rotation-invariant convolutional neural networks for object detection in vhr optical remote sensing images," *IEEE transactions on geoscience and remote sensing*, vol. 54, no. 12, pp. 7405–7415, 2016.

[22] G.-S. Xia, X. Bai, J. Ding, Z. Zhu, S. Belongie, J. Luo, M. Datcu, M. Pelillo, and L. Zhang, "Dota: A large-scale dataset for object detection in aerial images," in *Proceedings of the IEEE conference on computer vision and pattern recognition*, 2018, pp. 3974–3983.

[23] Y. Zhang, Y. Yuan, Y. Feng, and X. Lu, "Hierarchical and robust convolutional neural network for very high-resolution remote sensing object detection," *IEEE Transactions on Geoscience and Remote Sensing*, vol. 57, no. 8, pp. 5535–5548, 2019.

[24] C. Dong, C. C. Loy, K. He, and X. Tang, "Image super-resolution using deep convolutional networks," *IEEE transactions on pattern analysis and machine intelligence*, vol. 38, no. 2, pp. 295–307, 2015.

[25] S. Lei, Z. Shi, and Z. Zou, "Super-resolution for remote sensing images via local-global combined network," *IEEE Geoscience and Remote Sensing Letters*, vol. 14, no. 8, pp. 1243–1247, 2017.

[26] K. Jiang, Z. Wang, P. Yi, J. Jiang, J. Xiao, and Y. Yao, "Deep distillation recursive network for remote sensing imagery super-resolution," *Remote Sensing*, vol. 10, no. 11, p. 1700, 2018.

[27] K. Jiang, Z. Wang, P. Yi, G. Wang, T. Lu, and J. Jiang, "Edge-enhanced gan for remote sensing image superresolution," *IEEE Transactions on Geoscience and Remote Sensing*, vol. 57, no. 8, pp. 5799–5812, 2019.

[28] K. Jiang, Z. Wang, P. Yi, and J. Jiang, "Hierarchical dense recursive network for image super-resolution," *Pattern Recognition*, vol. 107, p. 107475, 2020.

[29] Y. Xiao, Q. Yuan, K. Jiang, J. He, Y. Wang, and L. Zhang, "From degrade to upgrade: Learning a self-supervised degradation guided adaptive network for blind remote sensing image super-resolution," *Information Fusion*, vol. 96, pp. 297–311, 2023.

[30] Y. Zhang, K. Li, K. Li, L. Wang, B. Zhong, and Y. Fu, "Image super-resolution using very deep residual channel attention networks," in *Proceedings of the European conference on computer vision (ECCV)*, 2018, pp. 286–301.

[31] B. Niu, W. Wen, W. Ren, X. Zhang, L. Yang, S. Wang, K. Zhang, X. Cao, and H. Shen, "Single image super-resolution via a holistic attention network," in *European conference on computer vision*. Springer, 2020, pp. 191–207.

[32] S. Lei and Z. Shi, "Hybrid-scale self-similarity exploitation for remote sensing image super-resolution," *IEEE Transactions on Geoscience and Remote Sensing*, vol. 60, pp. 1–10, 2022.

[33] Y. Mei, Y. Fan, and Y. Zhou, "Image super-resolution with non-local sparse attention," in *Proceedings of the IEEE/CVF conference on computer vision and pattern recognition*, 2021, pp. 3517–3526.

[34] B. Kim, J. Kim, and J. C. Ye, "Task-agnostic vision transformer for distributed learning of image processing," *IEEE Transactions on Image Processing*, vol. 32, pp. 203–218, 2022.

[35] J. He, Q. Yuan, J. Li, Y. Xiao, X. Liu, and Y. Zou, "Dster: A dense spectral transformer for remote sensing spectral super-resolution," *International Journal of Applied Earth Observation and Geoinformation*, vol. 109, p. 102773, 2022.

[36] Y. Xiao, Q. Yuan, K. Jiang, X. Jin, J. He, L. Zhang, and C.-w. Lin, "Local-global temporal difference learning for satellite video super-resolution," *IEEE Transactions on Circuits and Systems for Video Technology*, vol. 34, no. 4, pp. 2789–2802, 2023.

[37] J. Liang, J. Cao, G. Sun, K. Zhang, L. Van Gool, and R. Timofte, "Swinir: Image restoration using swin transformer," in *Proceedings of the IEEE/CVF international conference on computer vision*, 2021, pp. 1833–1844.

[38] Y. Xiao, Q. Yuan, K. Jiang, J. He, C.-W. Lin, and L. Zhang, "Ttst: A top-k token selective transformer for remote sensing image super-resolution," *IEEE Transactions on Image Processing*, vol. 33, pp. 738–752, 2024.

[39] X. Kang, P. Duan, J. Li, and S. Li, "Efficient swin transformer for remote sensing image super-resolution," *IEEE Transactions on Image Processing*, vol. 33, pp. 6367–6379, 2024.

[40] Z. Deng, H. Sun, S. Zhou, J. Zhao, L. Lei, and H. Zou, "Multi-scale object detection in remote sensing imagery with convolutional neural networks," *ISPRS Journal of Photogrammetry and Remote Sensing*, vol. 145, pp. 3–22, 2018.

[41] J. Wu, Z. Pan, B. Lei, and Y. Hu, "Fsanet: Feature-and-spatial-aligned network for tiny object detection in remote sensing images," *IEEE Transactions on Geoscience and Remote Sensing*, vol. 60, pp. 1–17, 2022.

[42] T. Shi, J. Gong, J. Hu, X. Zhi, W. Zhang, Y. Zhang, P. Zhang, and G. Bao, "Feature-enhanced centernet for small object detection in remote sensing images," *Remote Sensing*, vol. 14, no. 21, p. 5488, 2022.

[43] W. Lu, S.-B. Chen, H.-D. Li, Q.-L. Shu, C. H. Ding, J. Tang, and B. Luo, "Legnet: A lightweight edge-gaussian network for low-quality remote sensing image object detection," in *Proceedings of the IEEE/CVF International Conference on Computer Vision (ICCV) Workshops*, 2025, pp. 2844–2853.

[44] Y. Chen, B. Liu, and L. Yuan, "Pr-deformable detr: Detr for remote sensing object detection," *IEEE Geoscience and Remote Sensing Letters*, vol. 21, pp. 1–5, 2024.

[45] J. Shermeyer and A. Van Etten, "The effects of super-resolution on object detection performance in satellite imagery," in *2019 IEEE/CVF Conference on Computer Vision and Pattern Recognition Workshops (CVPRW)*, 2019, pp. 1432–1441.

[46] H. Ji, Z. Gao, T. Mei, and B. Ramesh, "Vehicle detection in remote sensing images leveraging on simultaneous super-resolution," *IEEE Geoscience and Remote Sensing Letters*, vol. 17, no. 4, pp. 676–680, 2019.

[47] J. Wu and S. Xu, "From point to region: Accurate and efficient hierarchical small object detection in low-resolution remote sensing images," *Remote Sensing*, vol. 13, no. 13, p. 2620, 2021.

[48] H. Zhang, F. Li, S. Liu, L. Zhang, H. Su, J. Zhu, L. M. Ni, and H.-Y. Shum, "Dino: Detr with improved denoising anchor boxes for end-to-end object detection," 2022.

[49] Z. Liu, Y. Lin, Y. Cao, H. Hu, Y. Wei, Z. Zhang, S. Lin, and B. Guo, "Swin transformer: Hierarchical vision transformer using shifted windows," in *Proceedings of the IEEE/CVF international conference on computer vision*, 2021, pp. 10 012–10 022.

[50] O. Ronneberger, P. Fischer, and T. Brox, "U-net: Convolutional networks for biomedical image segmentation," in *International Conference on Medical image computing and computer-assisted intervention*. Springer, 2015, pp. 234–241.

[51] T.-Y. Lin, P. Goyal, R. Girshick, K. He, and P. Dollár, "Focal loss for dense object detection," in *Proceedings of the IEEE international conference on computer vision*, 2017, pp. 2980–2988.

[52] Z. Cai and N. Vasconcelos, "Cascade r-cnn: Delving into high quality object detection," in *Proceedings of the IEEE conference on computer vision and pattern recognition*, 2018, pp. 6154–6162.

[53] Z. Ge, S. Liu, F. Wang, Z. Li, and J. Sun, "Yolox: Exceeding yolo series in 2021," *arXiv preprint arXiv:2107.08430*, 2021.

[54] P. Sun, R. Zhang, Y. Jiang, T. Kong, C. Xu, W. Zhan, M. Tomizuka, Z. Yuan, and P. Luo, "Sparse r-cnn: An end-to-end framework for object detection," *IEEE transactions on pattern analysis and machine intelligence*, vol. 45, no. 12, pp. 15 650–15 664, 2023.

[55] J. Wu, Z. Pan, B. Lei, and Y. Hu, "Fsanet: Feature-and-spatial-aligned network for tiny object detection in remote sensing images," *IEEE Trans. Geosci. Remote Sens.*, vol. 60, pp. 1–17, 2022.

[56] J. Zhang, J. Lei, W. Xie, Z. Fang, Y. Li, and Q. Du, "Superyolo: Super resolution assisted object detection in multimodal remote sensing imagery," *IEEE Transactions on Geoscience and Remote Sensing*, vol. 61, pp. 1–15, 2023.